Design and Characterization of the Fully Metallic Gap Waveguide based Frequency Selective Radome for Millimeter Wave Fixed Beam Array Antenna

Wai Yan Yong, *Graduate Student Member, IEEE*, Abolfazl Hadaddi, and Andrés Alayón Glazunov, *Senior Member, IEEE*

***Abstract*—This paper presents a bandpass frequency selective surface (FSS) radome based on fully metallic gap waveguide (GW) technology. The element of the proposed FSS radome consists of a conventional cross-dipole slot etched on metallic plates and positioned over a groove GW cavity. A design with a single GW cavity layer was initially produced which was later optimised for performance, to comprise a dual GW cavity layer, while considering both functionality and manufacturability. It is shown that the proposed FSS element offers a stable and wide bandpass (from 26-30 GHz) performance in the broadside direction for both transverse electric (TE) and transverse magnetic (TM) polarizations. For oblique angle of incidence, the suggested FSS element works up to 30° with a reduction in usable bandpass bandwidth performance to 26-28 GHz for both TE and TM polarizations. A 20×20-element GW-FSS array prototype has been fabricated and measured, which was integrated with a fixed beam array antenna to further validate its functionality as a filtering radome. The findings show an excellent agreement between simulations and measurements. Hence, the proposed GW-FSS represents a great opportunity to develop a all-metallic FSS with low insertion loss, sharp-roll-off filtering, wideband performance and inexpensive fabrication cost.**

***Index Terms*—Array antenna, Bandpass filtering, Frequency Selective Surface (FSS), Gap Waveguide, Radome**

I. Introduction

FREQUENCY selective surfaces (FSSs) are a type of periodic array structures that may be composed of radiating or non-radiating elements [1]. They have been widely used in a variety of applications including spatial filters [2], [3], polarisation converters [4], and reflect/transmit arrays antennas [5], [6]. Conventionally, FSSs are manufactured with periodic metallic layers with embedded substrates in-between. Substrate-based FSSs are critical to achieve desired filtering and selectivity (sharp roll-off) characteristics while at the same time they are simple to design and fabricate. However, they do not always provide the required high selectivity for the stopband rejection performance to attenuate the spurious signals. Numerous studies have been conducted to obtain the sharp roll-off with substrate-based FSS. One of the most used techniques is to increase the order of the FSS filter by realising the FSS with multilayer structures [3], [7]. Recently, it has also been suggested that the FSS can be designed in 3D to improve its filtering capability [8], [9]. These FSS structures do promise superior performance in terms of, e.g., high-order filtering response and larger bandwidth, particularly at the low frequency bands like the X-band. However, at higher frequencies, e.g., at the millimeter-wave (mmWave) range, these design methodologies may not be as efficient. For example, producing high-order FSS filters requires the use of a large number of substrates, which will lead to significant dielectric losses at mmWaves. Furthermore, the utilisation of 3D FSS structures poses a considerable challenge in manufacturing since the dimension of the FSS structures are considerably reduced at the mmWave bands. As a result, most if not all of these works [8], [9], have mainly found applications in the X-band or below.

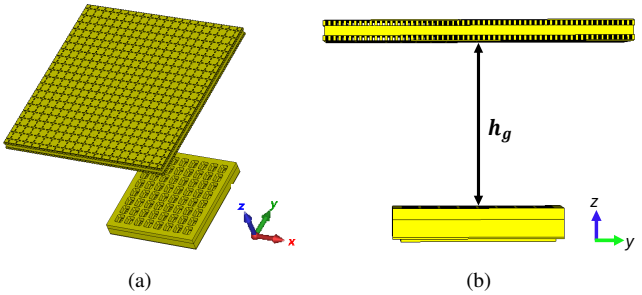

(a) (b)

Fig. 1: Artist representation of the proposed bandpass gap-waveguide based FSS integrated with the fixed beam array antenna. (a) Perspective view and (b) side view.

Lately, there has been a growing interest in exploring the mmWave and the THz bands for various applications such as 5G and beyond mmWave systems, connectivity, satellite communication, and vehicular radar applications [10], [11]. To deal with the aforementioned issues it has been proposed to design FSSs using the substrate integrated waveguide (SIW) technology [12]–[14]. The primary benefits of employing the SIW technology include improved loss performance in the mmWave band as well as increased power handling capacity [13], [14]. Furthermore, the use of the SIW cavity in the design

This project has received funding from the European Union's Horizon 2020 research and innovation programm under the Marie Sklodowska-Curie grant agreement No. 766231 — WAVECOMBE — H2020-MSCA-ITN-2017. (*Corresponding author: Wai Yan Yong.*)

W.Y.Yong is with Department of Electrical Engineering, University of Twente, 7500AE Enschede, Netherlands (e-mail: w.y.yongwaiyan@utwente.nl).

A.Hadaddi is with Gapwaves AB, Nellickevagen 22, 412 63 Gothernburg, Sweden (e-mail: abolfazl.haddadi@gapwaves.com).

A.A.Glazunov is with Department of Electrical Engineering, University of Twente, 7500AE Enschede, Netherlands and also with Department of Electrical Engineering, Chalmers University of Technology, 41296 Gothenburg, Sweden (e-mail: a.alayonglazunov@utwente.nl).

of the FSS allows for a high filtering performance even with single layer substrates [12]. However, dielectric losses in SIW are inevitable, especially as the frequency increases. For that reason, there has been an increasing interest in developing FSS radomes utilising *all-metallic* layers without a substrate [15], [16]. Nonetheless, owing to two primary factors, relatively few works have presented the design of FSSs based on an all-metallic solution. First, the mechanical considerations of the entirely metallic FSS do not allow for non-connected elements, as in substrate-based solutions, limiting its design freedom. Although design flexibility has recently increased with the emergence of 3D printing technology, its application to completely metallic structures (while showing behavioral agreement between designed and measured performance) is still not competitive in terms of dimensional tolerance and surface roughness [17]. Second, the miniaturisation of the unit cell periodicity is challenging since the permittivity-driven miniaturisation is not possible for all-metallic FSS structures.

Recently, the gap waveguide (GW) technology has shown to be a promising low-loss and low-cost mmWave transmission line and packaging technology. The physical principle of the GW is based on the parallel-plate waveguide concept [18]. While the GW cavity's performance is equivalent to that of a typical metallic waveguide, it can be realized at a lower cost [18], [19]. Furthermore, the GW technology enables the fabrication and operation of multilayer structures, providing great freedom in the design of the FSS. To the best of the authors' knowledge, no FSS structure based on GW technology has yet been suggested and investigated in the published literature.

Therefore, in this paper, we propose to design a low loss bandpass FSS radome for the mmWave band based on the GW technology. To demonstrate the advantages of our proposed GW-FSS solution, we present the design starting from the conventional cross-dipole slot over two metallic screens and the cross-dipole over the waveguide (WG) cavity and later transformed into the FSS based on the GW technology. Furthermore, a dual cavity GW-FSS is designed based on the single GW-cavity FSS with considerations of both manufacturability and filtering performance. After carefully optimising all of the parameters of the proposed GW-FSS, we integrated the FSS with the fixed beam array antenna presented in [20] to further validate the proposed GW-FSS as the filtering radome. We further investigate the impact of the GW-FSS on the performance of the array antenna in both pass and rejection band of the FSS. For this purpose, a 20×20 array prototype of the FSS is manufactured using two distinct materials with corresponding manufacturing technologies to lower manufacturing costs. Because of the advantages provided by the GW technology, these multilayer structures may be efficiently cascaded without concern for their electrical connection performance between one layer to another. Our experiments showed an excellent agreement with the proposed FSS.

The current concept is not only appropriate for mmWave applications, but it also opens up a new opportunity to investigate the implementation of these all-metallic FSS based on the GW technology for harsh environments such as military outdoor platforms and space applications. Because these FSS are built of metal, the power handling capabilities of the GW groove cavity is equivalent to that of conventional WG technology, which is typically used in these applications. Furthermore, thanks to the GW technology, the FSS structure may be simply built and produced into higher order FSS filters with multiple layers of metallic plates, depending on the attenuation level required by the applications. The GW-based bandpass FSS is presented for the first time in this paper. The suggested FSS has been designed as a promising candidate for bandpass filtering radome for fixed-beam array antennas.

The reminder of this article is arranged as follows. Section II outlines the progression of the design techniques used to achieve the proposed GW-based FSS, as well as its integration with the fixed beam array antenna. The experimental validation of a manufactured prototype is presented in Section III. The study also includes a comparison of the proposed work to the previously published FSS design and a discussion of drawbacks and benefits of the different techniques. Recommendations for future work are also given. Lastly the conclusions of the proposed work are summarized in Section IV.

II. Design Concepts

An artist representation of the designed bandpass GW-FSS integrated with array antenna is depicted in Fig 1. In this section we will consider several different types of FSS elements to demonstrate the benefits of GW-FSS design as well as a progression in the design process. Fig 2 shows the three considered designs, the fist one (a) is based on cross-dipole with two metallic plate layers, the second (b) is the metallic WG cavity-based FSS, and the third and main design (c) is the GW-FSS. The cross-dipole slot was chosen because it has been extensively studied in substrate-based FSS as a polarization-insensitive structure. The equivalent circuit model (ECM) of the cross-dipole and their operating principle is readily found in [1]. Moreover, it can be readily milled or etched on completely metallic plates without introducing the mechanical issues in the fabrication of the FSS structure as the uncut area of the unit cell is connecting to the next unit cell. The performance of the three FSS-element concepts is compared next based on simulated $S-$parameters.

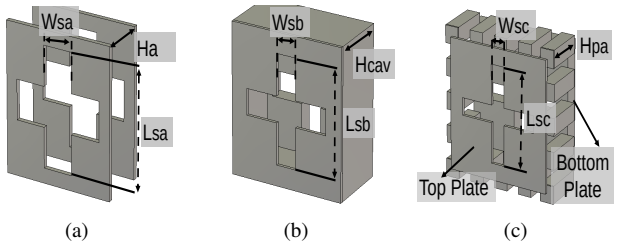

Fig. 2: Configuration of the cross-dipole FSS elements. (a) Conventional dual layer metal plate FSS, (b) Cross-dipole based on metallic WG cavity, and (c) Single Layer GW-FSS.

A. Conventional all-metallic FSS and WG cavity-based FSS

The design of the completely metallic FSS based on the metallic two-layer cross-dipole slot begins with the slot di-

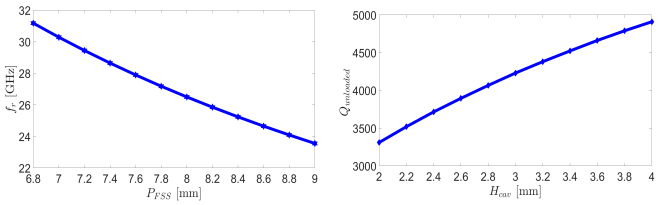

(a) (b)

Fig. 3: Simulated performance of the WG cavity. (a) Resonance frequency, f_r of the WG cavity with different FSS unit cell periodicity, P_{FSS} and (b) Unloaded Quality Factor, Q_{unloaded} with different cavity height, H_{cav}.

mensions, W_{sa} and L_{sa}, and the separation distance between the two metal plates H_a, which are indicated in Fig. 2(a) [15]. The resonance frequency of the slot where most of the incident EM energy is coupled to the structure is proportional to the overall slot length, which is approximately $0.5\lambda_f$, where λ_f is the wavelength at the center frequency [1]. Thus, the unit cell dimension is first set to 8 mm ($\approx 0.8\lambda$ at 30 GHz, the highest targeted operating frequency of the proposed FSS) to ensure it is sufficiently large to accommodate the cross-dipole slot operating at center frequency, f_c = 28 GHz, as well as providing some room for tuning the width, W_{sa} and length, L_{sa} of the slots, without the need of concern of the unwanted grating lobes. By optimising these parameters, a good insertion loss (IL) and reflection coefficient performance can be accomplished.

In the second design we've added the metallic cavity to the dual layer metallic FSS screen as shown in Fig. 2(b). The performance of the WG-cavity-based FSS is now affected by both the slot and the WG-cavity dimension. When a WG cavity is added to a dual layer metallic FSS screen, the equivalent impedance of the FSS's unit cell structure changes. This changes in the impedance is the result of the additional inductance effect in the ECM of the cross-dipole FSS contributed by the cavity resonator [21]. Therefore, results in an alteration in the FSS's transmission and reflection coefficients performance [12].

To design the WG cavity-based FSS, we must first consider the WG cavity's resonance frequency. The resonance frequency of the WG cavity exciting TE_{mnl} and TM_{mnl} modes is given by the well-known expression [21], $f_r = c/2\pi\sqrt{\mu_r\epsilon_r}\sqrt{(m\pi/a)^2 + (n\pi/b)^2 + (l\pi/d)^2}$, where a, b and d are the lengths of the cavity in the $x-$, $y-$, and $z-$directions, respectively. μ_r is the permeability, ϵ_r is the permittivity of the materials filling the WG resonator and c is the light velocity in vacuum. The dimensions a and b are dictated in our design by the periodicity of the unit cell denoted by the parameter P_{FSS}, and d is the height of the WG cavity which is indicated as H_{cav} in Fig. 2(b). Considering the slot structure dimensions and the need for a f_r in the desired operating frequency range of around 28 GHz, the WG resonator is chosen to excite in TM_{110} mode.

Fig. 3 illustrates the simulated resonant frequency and Q-factor of the WG cavity. As can be seen from Fig. 3(a), the f_r of the WG cavity depends on the cavity's width and length, which are denoted in our case by P_{FSS}. As P_{FSS} increases, the resonance frequency of the WG cavity decreases. It's worth noting that in our simulation, the H_{cav} has no discernible effect on the f_r of the WG resonator, therefore we have omitted it. On the other hand, H_{cav} has a noticeable effect on the quality factor Q_{unloaded} of the unloaded WG resonator. The Q_{unloaded} parameter is a measure of a resonator's losses, the higher Q_{unloaded} the lesser the losses and vice-versa [21]. In addition, Q_{unloaded} of the WG resonator and its bandwidth are inversely proportional $BW \propto 1/Q_{\text{unloaded}}$. As can be seen from Fig. 3(b), as H_{cav} increases, Q_{unloaded} increases too. It is critical to note that, the simulated f and Q_{unloaded} is for the unloaded case. When the FSS slots are loaded, the f_r and the Q_{loaded} values will change. f_r and Q_{unloaded} are metrics that may enable us to simply optimise the FSS's performance based on their dependence on the design parameters such as the dimensions of the FSS elements. The final dimension of the dual layer metallic FSS and WG cavity FSS are tabulated in Table. I.

TABLE I: Dimensions of Conventional Dual Layer Metallic FSS and WG cavity FSS (Refers to Fig. 2(a) and 2(b))

Parameters	Dimension [mm]
Conventional Dual Layer Metallic FSS	
Width of the slot, W_{sa}	2
Length of the slot, L_{sa}	6
Seperation between two metal plate, H_a	3
WG Cavity FSS	
Width of the slot, W_{sb}	1.4
Length of the slot, L_{sb}	5.8
WG cavity height, H_{cav}	3

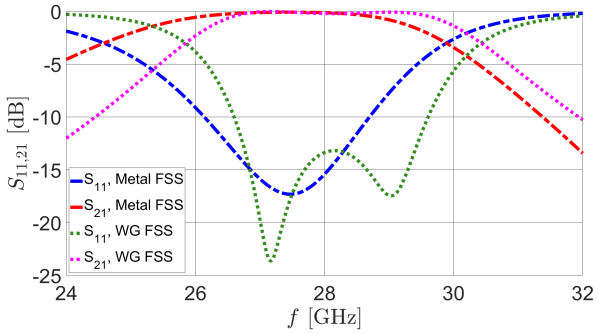

Fig. 4: Simulated $S-$parameters of the conventional dual layer metal plate FSS and WG cavity based FSS.

Fig. 4 illustrates the simulated transmission and reflection coefficient performance of the dual layer all-metallic FSS and the FSS based on WG cavity. As can be seen from Fig. 4, although a good bandwidth and low IL can be achieved by the dual metallic layer FSS, the filtering performance is just comparable to the conventional substrate-based FSS [1]. Clearly, the roll-off in the FSS's rejection band is not as steep. It is worth mentioning that the number of layers and the distance between the FSS metal plates have a considerable impact on its bandwidth and filtering performance. For example, increasing the number of FSS layers may improve the roll-off and bandwidth performance. However, the design of

the dual/multi-layer metallic FSS screen is not the primary objective of this study. However, in order to facilitate the comparison, with the single WG cavity FSS, we limit the number of metallic layers to two. The spacing between them H_a will later be equal to the cavity height of the WG cavity-based FSS H_{cav}. Moreover, to ensure a fair comparison, we optimised the final unit cell dimension of all three FSS structures in Fig. 2 to the same dimension.

The FSS slot's simulated $S-$parameter performance across the WG resonator is shown in Fig. 4. As can be seen, the WG cavity-based FSS provides two resonances rather than a single resonance, in comparison to the conventional dual layer metal plate FSS. This is due to an extra resonance frequency contributed by the WG cavity. It is worth mentioning that even if the WG cavity's resonance exists the slot structure is behaving as a bandstop structure, matching of the FSS unit cell remains impossible. Thus, the bandwidth performance of the all-metallic FSS screen can only be greatly enhanced by modifying both the resonance produced by the slot structure and the WG cavity. Although these WG cavity-based FSSs offer superior performance, their manufacturing is very complex and costly. Therefore, it is hardly ever employed in the design of the FSS devices. This leads us to the next subsection wherewe will detail our proposed GW cavity-based FSS.

B. Single Cavity Layer GW-FSS

As shown in [19], the performance of the groove GW cavity is equivalent to the conventional WG cavity. Hence, the design guidelines of the GW cavity FSS are similar to those in the WG cavity FSS. The primary difference is that instead of metallic walls surrounding the cavity, artificial magnetic conductors (AMC) pins are used. The AMC pins are designed in accordance with the design rules specified in [18]. The dispersion diagram for the designed AMC pins is shown in Fig. 5. As can be noted, the designed AMC exhibits the appropriate bandstop behaviour from 25 – 70 GHz.

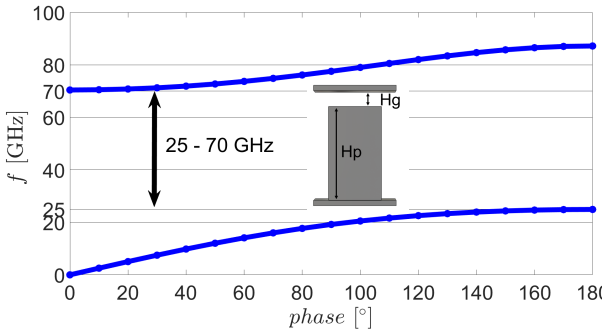

Fig. 5: Simulated dispersion diagram of the AMC pin for GW cavity.

As the first step in designing the GW-FSS, AMC pins are designed to replace the WG cavity wall. Afterwards, the final dimensions of the GW-cavity are optimised when the FSS slot are loaded using the CST unit cell simulation feature to obtain the desired bandwdith and filtering characteristics. As can be seen from Fig. 6, the performance of the GW cavity-based

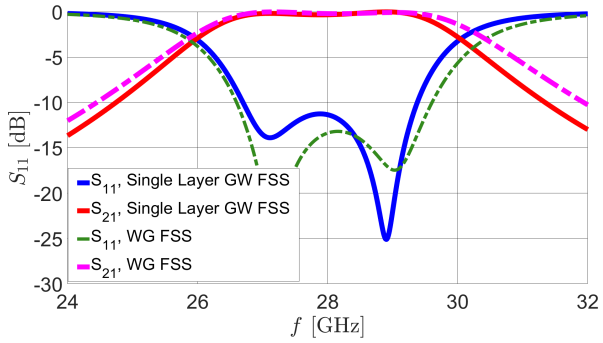

Fig. 6: Comparison of the siimulated $S-$parameters performance of the GW cavity FSS and WG cavity FSS.

FSS is comparable to that of the WG cavity-based FSS, where two resonances coexist, resulting in the wideband performance of this FSS structure. Moreover, the sharp roll-off over the rejection band can also be observed in GW cavity based FSS. In summary, the inclusion of metallic cavities (either WG or GW) allows for an improvement in the bandwidth performance as well as a sharper roll-off in the rejection band as compared to the design of completely metallic FSS screen alone.

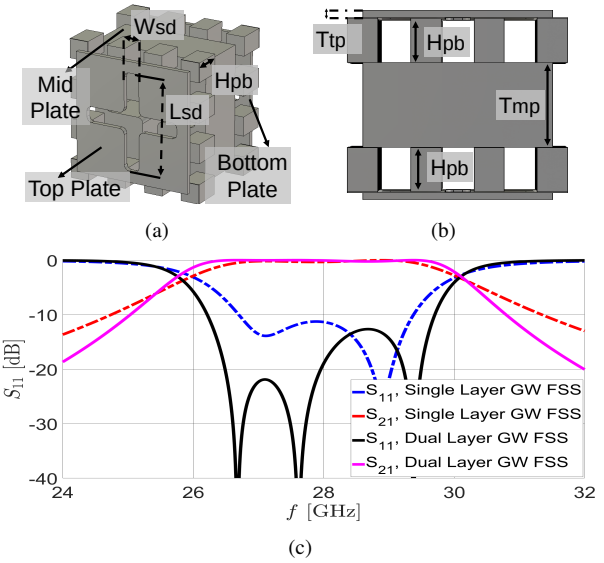

Fig. 7: Dual layer GW cavity cross-dipole FSS elements with (a) perspective view, (b) side view, and (c) Comparison simulated $S-$parameter for single layer and dual layer GW cavity FSS .

C. Dual Cavity Layer GW-FSS

Fig. 7 shows the proposed dual GW cavity FSS and the comparison of the simulated $S-$parameters for single and dual-layer GW cavity FSSs. Although the use of GW technology allows for lower WG cavity fabrication costs, there are particular rules that must be followed to simplify the production process and prevent substantial fabrication errors. One of the most important rules is that the metal plate on which the AMC pins are sitting must be sufficiently thick. This is to ensure that

TABLE II: Dimensions of Single layer and Dual Layer GW cavity FSS (Refers to Fig. 2(c) and 7).

Parameters	Dimension [mm]
Single layer GW Cavity FSS	
Width of the slot, W_{sc}	1.2
Length of the slot, L_{sc}	6
AMC Pin Height, H_{pa}	3
Dual Layer GW-FSS	
Width of the slot, W_{sd}	0.8
Length of the slot, L_{sd}	5.9
Height of the Mid Plate, T_{mp}	3

the mechanical strength of the metallic plate will support the manufacturing of the pins. However, if the metallic plate layer is too thick, machining the slot layers will be problematic. One option is to put AMC pins on both sides of the mid plate as illustrated in Fig. 8(b). In this case, milling can be applied on both sides of the surface. This approach also provides an opportunity for the manufacturing of the dual layer cavity FSS. The extra layer of the GW-cavity layer, like in standard substrate-based FSSs, will enhance the filtering order of the FSS, as they provide an additional inductance contribution over the FSS structure. This in turn will result in a sharper roll-off in the transmission coefficient [22]. As seen in Fig. 7(c), the inclusion of the extra GW cavity results in a steeper roll-off at both ends of the bandpass frequency (at 25 GHz and 30 GHz) which is consistent with the results reported in [22].

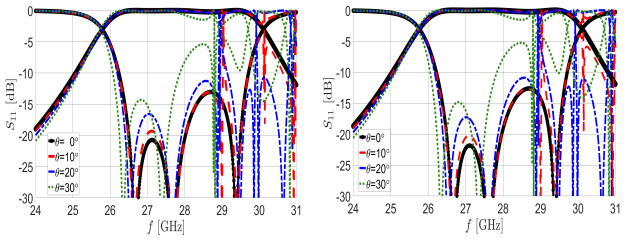

(a) (b)

Fig. 8: Simulated $S-$parameters at different angle of incidence for (a) TE and (b) TM polarization of the dual GW-cavity FSS.

Now, in order to determine the effectiveness of the suggested FSS as an antenna spatial filter, it is essential to analyse the structure's polarisation and angular stability performance. The simulated $S-$parameters of the dual GW cavity layer FSS at various angles of incidence for TE and TM polarisation are shown in Fig. 11. As can be seen from these plots, the performance of the TE and TM polarisations are indistinguishable as expected. Indeed, the suggested structure is polarisation insensitive as a result of the cross-dipole slot and the symmetrical design of the unit cell structure. On the other hand, as the incidence angle is scanned away from 0°, undesirable attenuation occurs at the upper end cut-off frequency. These undesired attenuation effects become more pronounced as the angle of incidence increases, resulting in a decrease in the usable bandwidth of the proposed FSS structure. The available bandwidth at 1 dB IL of the proposed FSS decreases from 14.3 % (26 – 30 GHz) at broadside to 8.1 % (26 – 28.1 GHz) at 30°. The FSS structure's angular instability is due to the huge unit cell dimension caused by the 0.5λ slot and the single waveguide cavity. This is a significant limitation of the all-metallic FSS radome, since miniaturisation resulted from the dielectric properties is unavailable as in the case with the conventional PCB-based FSS.

D. GW-FSS as the Filtering Radome for Array Antenna

The majority of the previous analyses were conducted utilising the CST software's unit cell boundary condition. To further evaluate the proposed GW-FSS as a filtering radome, Fig. 1 illustrates the integration of a finite 20×20 array of the FSS with the fixed beam wideband array antenna in [20]. The FSS structure is excited by an ideal plane wave in the simulation of the unit cell FSS. However, when the FSS is cascading with the array antenna designed in [20], the plane wave created by the array antenna in the near-field is non-ideal. Therefore, the near-field coupling effect between the array antenna and the FSS radome must be considered. One common approach is to further optimise the unit cell FSS in conjunction with the array antenna [23]. In this case, adjusting both the antenna and the FSS dimensions is particularly required. However, the design of the array antenna is not the major focus of our study, while on the other hand, we have demonstrated the functionality of our proposed FSS's as a filtering radome. Therefore, we do not performed any joint optimisation approach in our work. This leaves us with the option of finding the optimum distance between the already existing array antenna and the FSS radome, which has been computed using the open boundary condition in CST Microwave Studio. This strategy is not the best way to deal with this issue though. However, it might be used to reduce the influence of non-ideal plane waves on the FSS. Fig. 9 shows the simulated S_{11} with different distance, h_g (indicated in Fig. 1) between the array antenna and the FSS radome. As can be seen from Fig. 9, for $h_g \geq 10$ cm, the S_{11} of the array antenna with FSS radome remains below -10 dB from $26.5 - 29.8$ GHz. The chosen distance between the array antenna and the FSS radome is 13 cm.

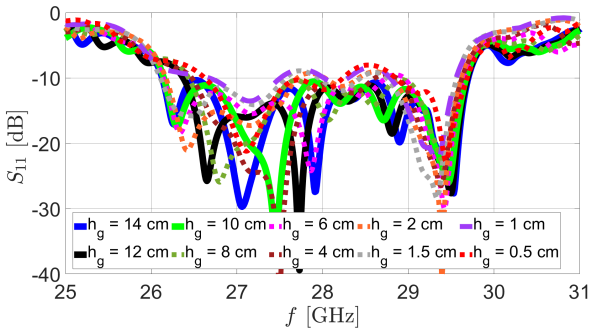

Fig. 9: Simulated S_{11} with different distance between the fixed beam array antenna (AA) designed in [20] and the dual GW-cavity FSS radome.

The Fig. 10 shows a comparison of the S_{11} performance for the fixed beam array antenna with and without the proposed

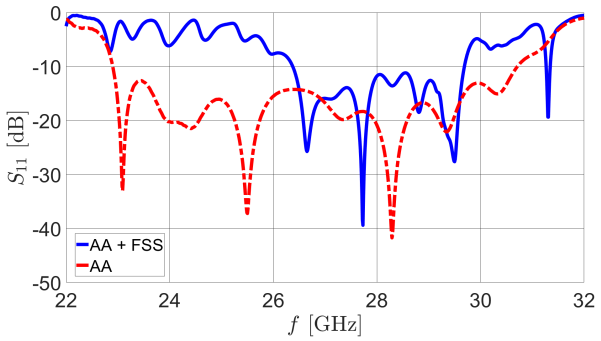

Fig. 10: Comparison of the simulated S_{11} for fixed beam array antenna (AA) designed in [20] with and without the dual GW-cavity FSS radome.

dual GW-cavity FSS radome. As can be seen from Fig. 10, the array antenna is well matched at less than -15 dB throughout the $23-31$ GHz frequency range. When the FSS radome is integrated with the antenna (with $h_g = 13$ cm), a significant mismatch occurs across the FSS radome's filtering band, i.e., ≤ 26.2 GHz and ≥ 29.8 GHz. This suggests that the designed FSS radome is acting as a filter, where most of the signals from the array antenna are unable to pass through the proposed FSS radome, and thus resulting in the array antenna mismatch. Furthermore, as shown in Fig. 10, the S_{11} performance is somewhat degraded from -15 dB to -12 dB in the passband of the FSS radome due to the non-ideal plane wave from array antenna as explained earlier. Therefore, if the FSS is manufactured for a specific antenna, then additional benefits may be realised with a joint optimisation approach.

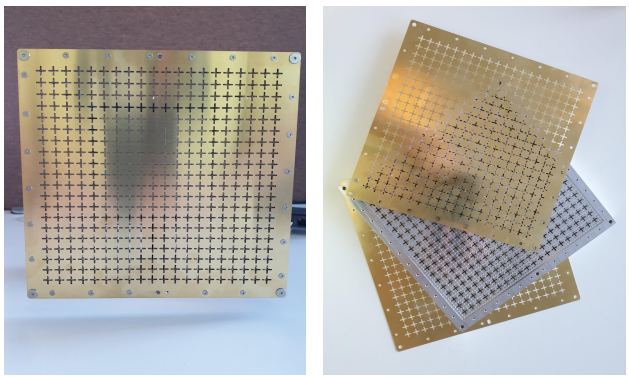

(a) (b)

Fig. 11: Fabricated prototype of the dual layer GW-cavity FSS with (a) front view and (b) explored view.

III. Experimental Results and Discussion

To validate the proposed GW-FSS, a prototype of an finite array with 20×20 elements was manufactured as shown in Fig. 11(b). The manufacturing of this FSS prototype incorporates two distinct fabrication methods and materials. The fundamental rationale for employing two separate manufacturing methods is to reduce fabrication costs. For example, the metallic chemical etching process used to manufacture the top and bottom metal plates is identical to PCB fabrication resulting in a cost-effective manufacturing solution. Although the etching production approach is by far more cost efficient, it cannot produce complicated 3D structures like the GW cavity, which comprises slots and AMC pins. On the other hand, the milling approach can achieve all three layers without any problems, but it is more expensive owing to the lengthy machining time. Therefore, the top and bottom metallic plates are made from Brass, CuZn37, see Fig. 7. We retain the final thickness of the top and bottom metallic plates at 0.3 mm in the design to account for both manufacturability and mechanical strength of the materials. Since this metallic plate is sufficiently thin (0.3 mm in our case), it may be manufactured utilising the chemical etching process. The mid plate, on the other hand, where the AMC pins and GW cavities are placed, is made of aluminium. This mid-plate is manufactured using a computer numerical control (CNC) milling process. Owing to the benefits of the GW technologies, these three layers can be cascaded together after the manufacturing process avoiding the air gap concerns that plague the majority of multi-layer FSS with cavity resonator designs. The manufactured FSS was tested both with and without integration to the fixed beam array antenna.

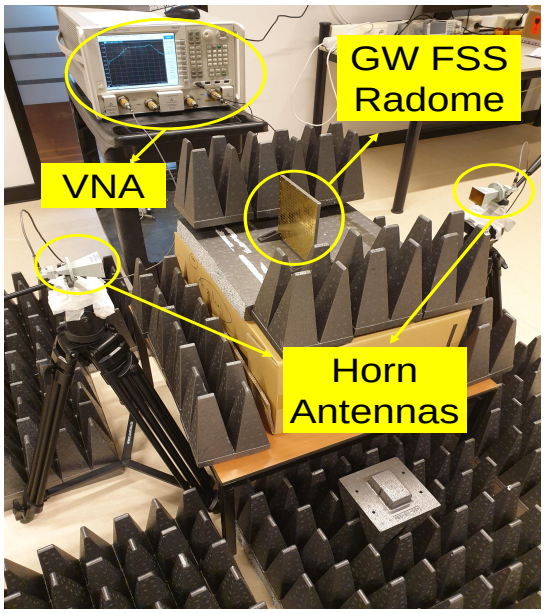

Fig. 12: Experimental setup for the evaluation of the transmission coefficient.

A. Evaluation of the Filtering Performance of the GW-FSS

To quantify the filtering performance of the proposed GW-FSS, a bi-static measurement setup was employed as shown in Fig. 12. Two identical standard horn antennas with 19 dBi gain were connected to a network analyzer in order to measure the transmission coefficient. The GW-FSS prototype was positioned between these horn antennas. It is worth mentioning that the minimum distance between the FSS prototype and the horn antenna must be positioned across the horn antenna's far-field region. This minimum separation distance between

the two horn antennas can be estimated from the Fraunhofer distance $d_{far-field} = 2D^2/\lambda_h$, where D is the horn antenna's maximum dimension and λ_h is the wavelength of the operating frequency [21]. For our case, the horn antenna with aperture size of $39.9 \times 47\ mm^2$, at 28 GHz, the far-field region of the horn antenna is around 42.5 cm. In our experiment, the FSS is placed at the center with two horn antenna seperated by 100 cm to ensure this far-field region is used.

The filtering performance characterization of the GW-FSS is carried out in free space. The comparison of the simulated and measured transmission coefficients of the proposed GW-FSS for broadside ($\theta = 0°$) is shown in Fig. 13. As can be seen, the manufactured FSS prototype has an IL ranging from 0.2 to 0.6 dB, which is about 0.3 dB higher than the simulation for both TE and TM polarization. This is primarily owing to the fact that simulations of FSS filtering performance were generally performed utilizing the unit cell boundary conditions in the CST, which do not account for IL due to edge effects for a finite array of the the FSS. Furthermore, the entire observed transmission coefficient is altered by around 0.2 GHz towards the higher frequencies for both the TE and TM polarizations. This is primarily due to the inevitable manufacturing imperfections. However, the transmission coefficient of the manufactured prototype is in good agreement with the simulated results. Furthermore, as anticipated by the simulations, the manufactured FSS has a sharp roll-off across the rejection band. For instance, at 26 GHz, the attenuation level is around 3 dB and is reduced to nearly 15 dB at 25 GHz. A similar observation can be made in the bandstop band at 31 GHz. Moreover, the measured transmission coefficient, S_{21} at different angles of incidence for the TE and TM polarizations is shown in Fig. 14. Similar to simulation results, when the angle of incidence deviate from $\theta = 0°$, an unwanted resonances is observed as a result of large periodicity of the FSS structure. Therefore, this unwanted resonance causes the reduction of the usable bandwidth of the proposed FSS structure at non-broadside direction.

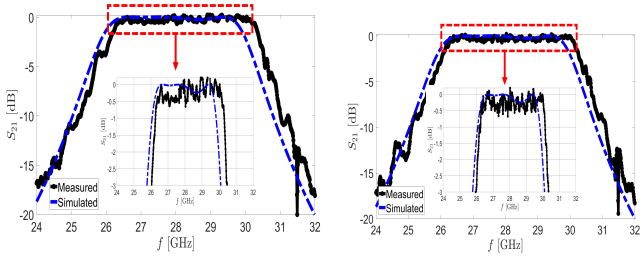

(a) (b)

Fig. 13: Comparison of the simulated and measured transmission coefficient, S_{21} at broadside ($\theta = 0°$) for (a) TE and (b) TM-polarization.

B. Investigation of the Fabrication Imperfections

As noted above, the measured transmission coefficient for the upper-end frequency is slightly altered by 0.2 GHz. To ascertain the cause of these minor shifts, we investigated and

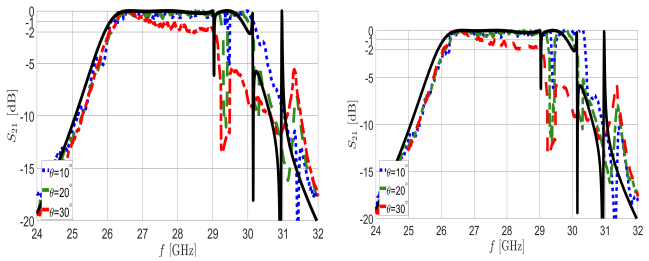

(a) (b)

Fig. 14: Measured transmission coefficient, S_{21} at different angle of incidence for (a) TE and (b) TM-polarization, where the black solid line is the simulated S_{21} at $\theta = 0°$ and the dotted lines are measured S_{21}.

TABLE III: Comparison of the simulated and fabricated dimensions of the proposed dual layer GW cavity FSS.(Refer to Fig. 7).

Parameters	Dimensions [mm]		
	Simulated	Measured (Etching)	Measured (Milling)
W_{sd}	0.8	0.859	0.835
L_{sd}	5.9	5.868	5.865
T_{tp}	0.3	0.35	N/A
Overall Thickness	7.6	7.7 (includes airgaps)	

analysed the dimensions of the manufactured FSS underneath the microscope. It's worth mentioning that, owing to the experimental facility limitations, certain simulated variables, such as the air gap and the AMC pin height, couldn't be reliably tested. Alternatively, we measured the overall thickness of the manufactured FSS prototype (comprising all the three metallic layers with the possible air gap between layers) using the micrometer screw gauge.

The simulated and fabricated dimensions for the proposed dual-layer GW-FSS are summarised in Table. III. We then used these measured values to evaluate the transmission coefficient performance of the FSS in CST. As can be seen in Fig. 15, when these FSS manufacturing imperfections are taken into account, the simulated transmission coefficient of the FSS becomes significantly more consistent with the experimental values. Some negligible deviations may still exist as a result of measurement errors and the aforementioned limitations on the inspection of fabrication inaccuracies.

C. Characterization of the GW-FSS as the Radome for a Fixed Beam Array Antenna

One of the primary functions of the proposed bandpass FSS is as a filtering radome for a fixed beam antenna. Therefore, we integrated the GW-FSS radome with the array antenna described in [20]. The filtering performance was experimentally validated. The manufactured prototype of the proposed GW-FSS integrated with the fixed beam array antenna is shown in Fig. 16.

The comparison of the simulated and measured S_{11} of the fixed beam array antenna with and without the FSS radome is shown in Fig. 17. The findings demonstrate that when the array

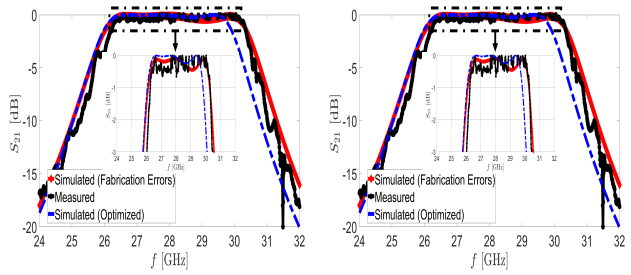

(a) (b)

Fig. 15: Comparison of the simulated and measured transmission coefficient of the FSS with taking into consideration of the fabrication error for (a) TE and (b) TM polarization.

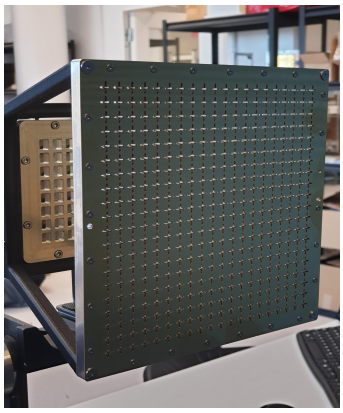

Fig. 16: Fabricated GW-FSS integrated with the fixed beam array antenna.

antenna is without the FSS radome has excellent impedance matching from 23 – 31 GHz at $S_{11} \leq -15$ dB. When the FSS radome is used with the array antenna, the overall matching performance of the array antenna degrades, either in the FSS passband (26.2 – 30.2 GHz) or in the rejection band ($f < 26.2$ GHz and $f > 30.2$ GHz). The array antenna's impedance matching performance degradation in the pass and rejection bands of the FSS can be accounted by two distinct factors. First, although the impedance matching of the integrated array antenna with the proposed FSS radome is not as excellent as it would be without the radome, the measured S_{11} is less than -10 dB over the pass band of the FSS radome. This performance fulfills the minimum required matching level for the array antenna to radiate adequately. Furthermore, as mentioned above, the proposed GW-FSS was not purposely developed for this particular array antenna. Thus, throughout the design phase, joint matching optimisation of the FSS with the antenna design as reported, e.g., in [23], was not performed during our design stage. Therefore, some impedance matching degradation in the passband was observed. In addition, as mentioned above, the IL of the GW-FSS prototype is around 0.2 – 0.6 dB, the deteriorating of impedance mismatch over the passband of the FSS radome should take these ILs into account. Nevertheless, it can be observed that the measured impedance mismatch over the bandpass is more significant than in the simulation which can be explained as follows. First,

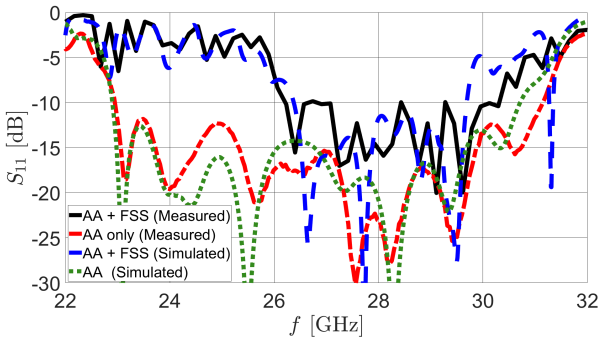

Fig. 17: Comparison of the simulated and measured S_{11} for fixed beam array antenna (AA) designed in [20] with and without the dual GW-cavity FSS radome.

based on the characterization of the FSS radome, we know that the insertion loss of the FSS prototype is approximately 0.3 dB higher than expected. This increased ILs will contribute to the mismatching of the measured reflection coefficient. Furthermore, the distance between the AA and the suggested FSS radome is fixed according to the simulation at $d = 13$ cm because of the limitations of our measurement setup. However, the optimal distance between the AA and the FSS may vary in actual prototyping. Therefore, the FSS radome might be mechanically re-moved and adjusted to find the optimum distance between AA and FSS. Another possible factor is the altering of the FSS radome's operating frequency as a result of fabrication errors. The impedance mismatching of the array antenna, on the other hand, is substantially more severe across the rejection band of the FSS radome. The array antenna's S_{11} has been increased from -15 dB to roughly > -4 dB. Unlike the above-mentioned matching degradation in the FSS radome's passband, this degradation of the S_{11} across the rejection band is caused by the FSS radome reflecting back the array antenna's signals. Thus, most of the signals are unable to pass through the FSS radome over the bandstop frequency of the FSS.

To offer a better understanding of the above arguments, the measured radiation patterns of the array antenna with and without the deployment of our proposed FSS radome are shown in Figs. 18 and 19 for the E- and H-planes, respectively. We can see from the measured radiation patterns that there is no substantial difference in the radiation pattern of the array antenna with or without the FSS radome across the pass band of the FSS radome. The GW-FSS is transparent to the array antenna in the passband, hence its impact on the array antenna radiation pattern is negligible. In contrast, the radiation pattern of the array antenna is clearly reduced in the rejection band of the GW-FSS, as can be seen from the measured radiation patterns at 24 and 31 GHz. These findings are therefore consistent with our prior explanation of the results of the array antenna's impedance mismatching reasoning when comparing the performance with and without the FSS radome. Moreover, the comparison of the simulated and measured gain of the array antenna with and without the GW-FSS radome is plotted in Fig. 20. The effects on antenna gain performance with the suggested FSS radome on the array

antenna are comparable to previous results. In the passband, the effect on antenna gain performance is negligible. However, the antenna gain drops dramatically in the rejection frequency, with a gain decrease of about 10 dBi.

We can therefore conclude that the integration of the GW-FSS may result in a degradation of overall impedance matching performance since the FSS has not been optimised in conjunction with the array antenna. However, degradation in the passband has no effect the on antenna performance as long as the impedance matching level remains below −10 dB. In contrast, a substantial mismatch on the array antenna occurred in the rejection band, and the array antenna performance is severely decreased in this region since the GW-FSS is preventing the signals from travelling through.

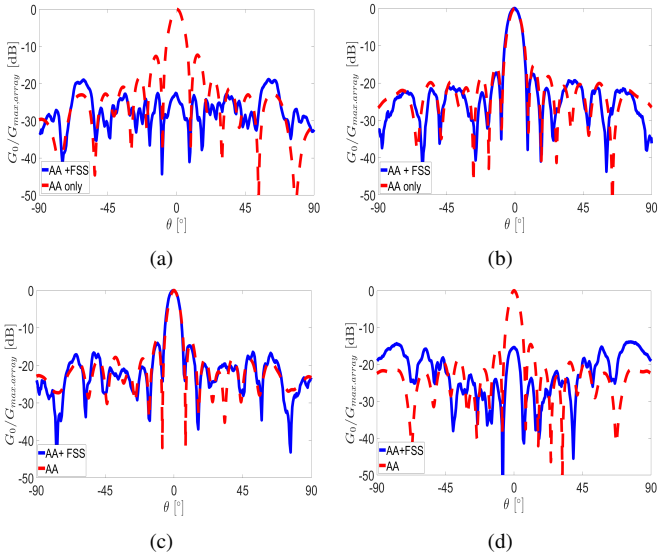

Fig. 18: Comparison of the measured E-plane radiation for the fixed beam array antenna (AA) with and without the proposed GW-FSS radome for (a) 24 GHz, (b) 27 GHz, (c) 28 GHz and (d) 31 GHz, where $G_0/G_{max,array}$ is the normalized antenna gain in dBi, $G_{max,array}$ is the maximum gain of the AA without radome and θ is the polar angle in degrees.

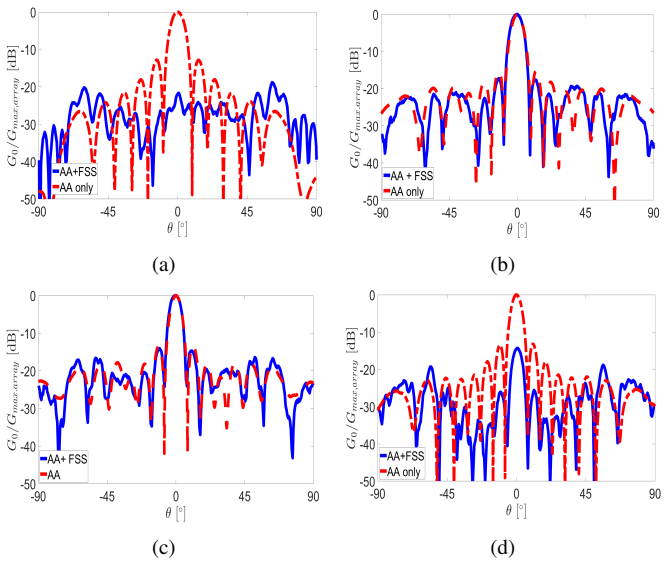

Fig. 19: Comparison of the measured H-plane radiation for the fixed beam array antenna (AA) with and without the proposed GW-FSS radome for (a) 24 GHz, (b) 27 GHz, (c) 28 GHz and (d) 31 GHz, where $G_0/G_{max,array}$ is the normalized antenna gain in dBi, $G_{max,array}$ is the maximum gain of the AA without radome and θ is the polar angle in degrees.

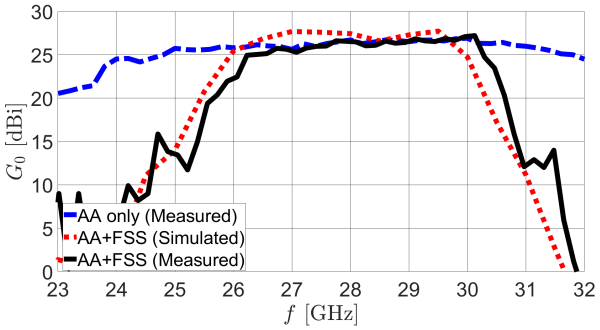

Fig. 20: Comparison of the simulated and measured gain, G_0 for fixed beam array antenna (AA) designed in [20] with and without the dual GW-cavity FSS radome.

D. Discussion

Table. IV compares numerous bandpass FSS based on different design methodologies. Emphasis should be put on the mmWave band. The IL for the PCB-based FSS is significant in the mmWave band, where the IL is higher than 3 dB at broadside when two layer of substrates are utilized in the design [3], [7]. Moreover, the IL increases with frequency. However, in terms of compactness, these PCB-based solutions have a substantial advantage. Filtering performance with good angular stability also may be achieved by designing the substrate-based FSS adequately [3]. Moreover, as discussed above, designing an FSS as a 3D structure is an alternate technique to designing an FSS with superior filtering performance [8]. However, because of the manufacturing complexity, the reported works are limited to low frequency bands. Therefore, despite the advances in 3D printing technology, which could resolve the manufacturing challenge, this form of 3D FSS is still mainly employed for low frequency applications [9]. Utilizing the SIW technology to design the FSS with superior filtering performance for high frequency is a better alternative. Indeed, the SIW cavity enables to obtain a sharp roll-off even with a single layer PCB, reducing the total dielectric losses [13]. The dielectric losses, however, remain unavoidable as the frequency increases. As shown in Table. IV, the IL of the SIW technology is about 0.35 dB at X-band [14] and increases dramatically to 2.5 dB in mmWave band [13]. It is crucial to note that all the compared works have a rapid roll-off across the rejection band, therefore it is not necessary to compare their band-rejection performance in the table.

On the other hand, there is a lot of interest in designing mmWave band FSS using all-metallic designs. It is worth noting that the key goal of several of these all-metallic FSS

TABLE IV: Performance comparison of existing FSS radome for mmWave applications. f is the operating frequency and IL is the insertion loss.

Ref.	f [GHz]	Unit Cell Periodicity	IL at broadside (dB)	Angular Stability	Design Methodology	Fabrication Technology	All-Metallic
[3]	24.72 – 30.24	$0.62\lambda_h$	3.23	up to 40°	Multi-layer PCB	PCB	No
[7]	33 – 35	$0.63\lambda_h$	3 – 3.5	up to 15°	Multi-layer PCB	PCB	No
[8]	3.1 – 3.7	$0.1\lambda_h$	≤ 0.5	up to 45°	3D FSS	PCB	No
[9]	3.24 – 5.52	$0.55\lambda_h$	1.2 – 4.4	up to 45°	3D FSS	3D Printing	No
[13]	29.5 – 30.5	$0.73\lambda_h$	2.5	up to 30°	SIW	PCB	No
[14]	9.5 – 10	$0.27\lambda_h$	0.35	up to 60°	SIW	PCB	No
[15]	27 – 30	$0.96\lambda_h$	≤ 0.7	Not Reported	Metal Plate only	Milling (Water cutting)	Yes
[16]	14.6 – 15.6	≤ $0.5\lambda_h$	≥ 3.2	up to 20°	waveguide	3D printing	Yes
[24]	19 – 29	$0.52\lambda_h$	1.2	up to 30°	TEM waveguide	3D printing	Yes
This Work	26.2 – 30.2	$0.76\lambda_h$	0.6	up to 20° with loss of 1 GHz BW	GW	Milling and Etching	Yes

is to design a polarisation converter or polarizer. Nonetheless, there has been little work presented [15], [16], [24] of all-metallic FSS, which results we have taken into account. Moreover, since the filtering response is not their primary design focus, most of these designs are not optimised for rapid roll-off performance across the bandstop frequencies. Due to the fact that these circular polarizers are typically designed as bandpass FSS, the IL loss and angular stability performance are critical for these operations. As a result, the IL and angular stability performance are adequate for our comparison. Compared to the substrate-based FSS, these all-metallic FSS give higher IL performance as expected. Hence, for all-metallic FSS, the unfavourable dielectric loss has been eliminated. Although all-metallic FSS may provide better loss performance, the unit cell dimensions are often larger than in substrate-based FSS because a permittivity-driven miniaturisation is not achievable with the all-metallic FSS solution. As a result, the angular stability performance of the all-metallic FSS is inferior to that of the substrate-based FSS. These unit cell dimension issues of the all-metallic FSS become less pronounced when the FSS is manufactured via 3D printing because of the higher design flexibility. In terms of milling and etching, the only viable structure is the slot structure, which considerably limits the design flexibility.

Furthermore, the IL performance of all-metallic FSS highly depends on the manufacturing technique. As shown in Table. IV, the prototype created utilising the milling technique outperforms 3D printing in terms of IL performance owing to better control over the surface roughness of the metallic layer in the fabrication. The fundamental issues with the 3D printing technology, as rigorously examined in [17], are the dimensional tolerance and the surface roughness. This is clearly demonstrated in [16] and [24], where the IL in the simulation for both of these FSS is less than 0.5 dB, whereas the observed IL for the manufactured FSS is 3.2 dB and 1.2 dB, respectively. Despite the fact that the study presented in [24] shows a considerable improvement in the 3D printed FSS, its IL performance remains can't be compared to the conventional milling technology. Furthermore, it is worth highlighting that when these FSS prototypes are manufactured utilising 3D printing, the IL performance of the substrate-based 3D FSS is still worse than the all-metallic FSS.

Compared to the fully metallic bandpass FSS radome in [15], our proposed GW-FSS offers a number of advantages. First, the use of GW technology in the construction of the bandpass FSS radome, which enables to share the inherent advantages of waveguides, similarly to the SIW-based FSS structures [12], such as its high power handling capacity, higher Q-factors, and improved filtering selectivity [19], which is not being offered by most of the fully metallic FSS structures presented today [15], [24]. For instance, as compared to [15] our proposed GW-FSS offered a better filtering selectivity. The transition band (from 3 dB IL to 10 dB IL) of the FSS radome presented in [15] is approximately 1.8 GHz, whereas the transition band of our proposed GW-FSS is only less than 1 GHz. Hence the use of GW technology in designing the FSS offers an improved filtering selectivity of the bandpass response.

In summary, to broaden the applications of all-metallic FSS, future research should concentrate on improving the performance of the all-metallic structure for greater oblique angles of incidence by miniaturising the unit cell size. Moreover, this task should be completed by taking into account the impact of manufacturing on IL performance. Finally, the design of the integrated all-metallic FSS and and an array antenna shall be carried out jointly.

IV. Conclusion

We have proposed a frequency selective surface (FSS) based on a fully metallic gap waveguide (GW) as a filtering radome for a mmWave fixed beam array antenna. For the first time, the FSS radome has been designed using the GW technology. Due to the use of the all-metallic GW technology, the proposed FSS exhibit excellent filtering performance with minimal insertion loss (IL) in the passband and a rapid roll-off throughout the rejection band. The low IL is primarily due to the absence of a substrate in the design, while the fast roll-off is a result of the GW cavity's contribution. Additionally, when the proposed FSS radome is combined with a wideband, high gain fixed beam array antenna, the radome's filtering characteristics remain intact. Within the passband of the proposed FSS, the array antenna's radiation pattern and antenna gain performance are equivalent to those obtained without the FSS radome. On the other hand, in the FSS's rejection band, the array antenna's radiation pattern and antenna gain performance degrade significantly. For oblique angles of incidence, as the

angle of incidence increases, an undesired resonance appears at the operational frequency's upper end, resulting in the FSS's usable bandwidth reduction by roughly 1 GHz. This is mostly due to the large unit cell size of the proposed FSS, which makes it sensitive to changes in the angle of incidence.

Although the current work demonstrates that this GW-FSS mainly performs well for broadside direction, the low IL, sharp roll-off performance, low manufacturing cost and mechanically robustness makes it attractive for a variety of applications. For example, of particular interest are the mmWave and THz bands, as well as applications in harsh environments such as military and satellite communications. Nevertheless, additional efforts will need to be made in future designs to take full advantage of the proposed novel approach to design all-metallic FSS structures. For instance, further research could look into the miniaturization of the unit cell dimensions in order to improve angular stability over a large bandwidths. The miniaturisation of the proposed GW-FSS must take into account two factors: the miniaturisation of the metallic slot and the miniaturisation of the GW-cavity. Moreover, more research must be undertaken to determine the strategy for broadening the bandwidth performance of the GW-FSS as well as further improving the filtering response of the suggested GW-FSS over broadside and oblique angles. Additionally, in order to broaden the applicability of these all-metallic GW-FSS, we should also investigate if they may be designated as circular polarisers.

ACKNOWLEDGMENTS

The authors would like to thank Gapwaves AB for fabricating the prototype, Daniel Johansson for the supports and discussion in the mechanical design and fabrication of the prototype and Alireza Bagheri for the helps in radiation pattern measurement.

REFERENCES

[1] B. A. Munk, *Frequency selective surfaces: theory and design*. John Wiley & Sons, 2005.

[2] W. Y. Yong, S. K. A. Rahim, M. Himdi, F. C. Seman, D. L. Suong, M. R. Ramli, and H. A. Elmobarak, "Flexible convoluted ring shaped FSS for X-band screening application," *IEEE Access*, vol. 6, pp. 11 657–11 665, 2018.

[3] D. Li, T.-W. Li, R. Hao, H.-S. Chen, W.-Y. Yin, H.-C. Yu, and E.-P. Li, "A low-profile broadband bandpass frequency selective surface with two rapid band edges for 5G near-field applications," *IEEE Transactions on Electromagnetic Compatibility*, vol. 59, no. 2, pp. 670–676, 2017.

[4] B. Lin, W. Huang, L. Lv, J. Guo, Z. Wang, and R. Zhu, "Second-order polarization rotating frequency-selective surface," *IEEE Transactions on Antennas and Propagation*, vol. 69, no. 11, pp. 7976–7981, 2021.

[5] K. Mavrakakis, H. Luyen, J. H. Booske, and N. Behdad, "Wideband transmitarrays based on polarization-rotating miniaturized-element frequency selective surfaces," *IEEE Transactions on Antennas and Propagation*, vol. 68, no. 3, pp. 2128–2137, 2019.

[6] P. Mei, G. F. Pedersen, and S. Zhang, "A broadband and FSS-based transmitarray antenna for 5G millimeter-wave applications," *IEEE Antennas and Wireless Propagation Letters*, vol. 20, no. 1, pp. 103–107, 2020.

[7] A. Abbaspour-Tamijani, K. Sarabandi, and G. M. Rebeiz, "Antenna-filter-antenna arrays as a class of bandpass frequency-selective surfaces," *IEEE transactions on microwave theory and techniques*, vol. 52, no. 8, pp. 1781–1789, 2004.

[8] A. A. Omar and Z. Shen, "Thin 3-D bandpass frequency-selective structure based on folded substrate for conformal radome applications," *IEEE Transactions on Antennas and Propagation*, vol. 67, no. 1, pp. 282–290, 2018.

[9] S. Qiu, Q. Guo, and Z. Li, "Tunable frequency selective surface based on a sliding 3d-printed inserted dielectric," *IEEE Access*, vol. 9, pp. 19 743–19 748, 2021.

[10] Y.-X. Sun, K. W. Leung, and K. Lu, "Compact dual microwave/millimeter-wave planar shared-aperture antenna for vehicle-to-vehicle/5G communications," *IEEE Transactions on Vehicular Technology*, vol. 70, no. 5, pp. 5071–5076, 2021.

[11] K. K. W. Low, S. Zihir, T. Kanar, and G. M. Rebeiz, "A 27-31-GHz 1024-Element Ka-Band SATCOM Phased-Array Transmitter With 49.5-dBW Peak EIRP, 1-dB AR, and±70° Beam Scanning," *IEEE Transactions on Microwave Theory and Techniques*, 2022 (Early Access).

[12] G. Q. Luo, W. Hong, Z.-C. Hao, B. Liu, W. D. Li, J. X. Chen, H. X. Zhou, and K. Wu, "Theory and experiment of novel frequency selective surface based on substrate integrated waveguide technology," *IEEE transactions on antennas and propagation*, vol. 53, no. 12, pp. 4035–4043, 2005.

[13] G. Q. Luo, W. Hong, Q. H. Lai, K. Wu, and L. L. Sun, "Design and experimental verification of compact frequency-selective surface with quasi-elliptic bandpass response," *IEEE transactions on microwave theory and techniques*, vol. 55, no. 12, pp. 2481–2487, 2007.

[14] H. B. Wang and Y. J. Cheng, "Frequency selective surface with miniaturized elements based on quarter-mode substrate integrated waveguide cavity with two poles," *IEEE Transactions on Antennas and Propagation*, vol. 64, no. 3, pp. 914–922, 2015.

[15] J. Lundgren, O. Zetterstrom, F. Mesa, N. J. Fonseca, and O. Quevedo-Teruel, "Fully Metallic Dual-Band Linear-to-Circular Polarizer for K/K a-band," *IEEE Antennas and Wireless Propagation Letters*, vol. 20, no. 11, pp. 2191–2195, 2021.

[16] C. M. Jimenez, E. Menargues, and M. García-Vigueras, "All-metal 3-d frequency-selective surface with versatile dual-band polarization conversion," *IEEE Transactions on Antennas and Propagation*, vol. 68, no. 7, pp. 5431–5441, 2020.

[17] B. Zhang, Y.-X. Guo, H. Zirath, and Y. P. Zhang, "Investigation on 3-D-printing technologies for millimeter-wave and terahertz applications," *Proceedings of the IEEE*, vol. 105, no. 4, pp. 723–736, 2017.

[18] P.-S. Kildal, E. Alfonso, A. Valero-Nogueira, and E. Rajo-Iglesias, "Local metamaterial-based waveguides in gaps between parallel metal plates," *IEEE Antennas and Wireless Propagation Letters*, vol. 8, pp. 84–87, 2009.

[19] E. Rajo-iglesias, M. Ferrando-rocher, and A. U. Zaman, "Gap Waveguide Technology for Millimeter-Wave Antenna Systems," *IEEE Communications Magazine*, vol. 56, no. July, pp. 14–20, 2018.

[20] W. Y. Yong, A. Haddadi, T. Emanuelsson, and A. A. Glazunov, "A bandwidth-enhanced cavity-backed slot array antenna for mmwave fixed-beam applications," *IEEE Antennas and Wireless Propagation Letters*, vol. 19, no. 11, pp. 1924–1928, 2020.

[21] D. M. Pozar, *Microwave engineering*. John wiley & sons, 2011.

[22] K. Sarabandi and N. Behdad, "A frequency selective surface with miniaturized elements," *IEEE Transactions on Antennas and propagation*, vol. 55, no. 5, pp. 1239–1245, 2007.

[23] D. Sánchez-Escuderos, M. Ferrando-Rocher, J. I. Herranz-Herruzo, and A. Valero-Nogueira, "Grating lobes reduction using a multilayer frequency selective surface on a dual-polarized aperture array antenna in Ka-Band," *IEEE Access*, vol. 8, pp. 104 977–104 984, 2020.

[24] C. Molero, H. Legay, T. Pierre, and M. Garcia-Vigueras, "Broadband 3D-Printed Polarizer based on Metallic Transverse Electro-Magnetic Unit-Cells," *IEEE Transactions on Antennas and Propagation*, 2022 (Early Access).

Wai Yan Yong (Graduate Student Member, IEEE) received the bachelor's degree (Hons.) in electronic engineering from the Universiti Tun Hussein Onn Malaysia (UTHM), Parit Raja, Malaysia, in 2016, and the M.Phil. degree in electrical engineering from Universiti Teknologi Malaysia (UTM), Johor Bahru, Malaysia, in 2018. Mr. Yong was a recipient of the UTHM Chancellor's Award during the 16th UTHM Convocation and the Best Postgraduate Student Award for his master's degree during the 60th UTM Convocation.

He is currently pursuing the D.Phil. degree with the Department of Radio System Engineering, University of Twente, Enschede, The Netherlands. He is currently the Marie Curie Researcher funded by the European Union through the Marie Currie Horizon 2020 Project. He is also a Visiting Researcher with Gapwaves AB, Gothenburg, Sweden. His research interests include, but not limited to, millimeter-wave and THz antenna array designs, frequency-selective surfaces, phased array transceivers, and new materials for antenna and microwave devices.

Abolfazl Haddadi received his PhD degree from Amir Kabir University of Technology, Tehran, Iran, in with a thesis entitled "Reflector Antenna Surface Distortions: Determination and Compensation". In March 2015, he was at Chalmers University of Technology, Sweden, as a visitor researcher, where he worked on the hat and the eleven array antennas. He had worked in a number of R&D roles for research institutes in Iran. In 2017, he joined Gapwaves AB in Sweden as a senior antenna design engineer. He is the author and co-author of more than 20 papers in various conferences and journals. His Main interests are automotive radars, mmWave antenna systems, satellite communications and 5G systems.

Andrés Alayón Glazunov (SM'11) was born in Havana, Cuba. He received the M.Sc. (Engineer-Researcher) degree in physical engineering from Peter the Great St. Petersburg Polytechnic University (Polytech), St. Petersburg, Russia, in 1994, the Ph.D. degree in electrical engineering from Lund University, Lund Sweden, in 2009, and the Docent (Habilitation) qualification in antenna systems from Chalmers University of Technology, Gothenburg, Sweden, in 2017. From 1996-2005, he held various research and specialist positions in the Telecom industry, e.g., Ericsson Research, Telia Research, and TeliaSonera, in Stockholm, Sweden. From 2001-2005, he was the Swedish delegate to the European Cost Action 273 and from 2018-2020 he was the Dutch delegate to the European Cost Action IRACON. He has been one of the pioneers in producing the first standardized OTA measurement techniques for 3GPP, and devising novel OTA techniques, e.g., the Random-LOS and the Hybrid antenna characterization techiques.

He has contributed to, or initiated various European research projects, e.g., more recently, the is3DMIMO, the WAVECOMBE, the 5VC and the Build-Wise projects under the auspices of the H2020 European Research and Innovation program. Dr. Glazunov has also contributed to the international 3GPP and the ITU standardization bodies. From 2009-2010, he held a Marie Curie Senior Research Fellowship at the Centre for Wireless Network Design, University of Bedfordshire, Luton, U.K. From 2010-2014, he held a post-doctoral position with the Electromagnetic Engineering Laboratory, KTH-Royal Institute of Technology, Stockholm, Sweden. From 2014-2018, he held an Assistant Professor position at Chalmers University of Technology, Gothenburg, Sweden.

Dr. Glazunov is currently an Associate Professor with the Department of Electrical Engineering, University of Twente, Enschede, the Netherlands, where he is leading the Antenna Systems, Propagation and OTA research. And he is also an Affiliate Associate Professor with the Chalmers University of Technology, Gothenburg, Sweden, where he is leading the OTA Characterization of Antenna Systems research area. He is the author of more than hundred and fifty scientific and technical publications. He is the co-author and co-editor of the text book LTE-Advanced and Next Generation Wireless Networks – Channel Modelling and Propagation (Wiley, 2012). His current research interests include, but are not limited to mmWave sensor array design, MIMO antenna systems, electromagnetic theory, fundamental limitations on antenna-channel interactions, radio propagation channel measurements, modeling and simulations, wireless performance in the built environment, and the OTA characterization of antenna systems and wireless devices.